Monthly Notices of the ROYAL ASTRONOMICAL SOCIETY

MNRAS **504,** 1495–1510 (2021)
Advance Access publication 2021 March 25

doi:10.1093/mnras/stab854

The effect of the streaming instability on protoplanetary disc emission at millimetre wavelengths

Chiara E. Scardoni,[1★] Richard A. Booth [1,2] and Cathie J. Clarke[1]

[1] *Institute of Astronomy, University of Cambridge, Madingley Road, Cambridge CB3 0HA, UK*
[2] *Astrophysics Group, Imperial College London, Blackett Laboratory, Prince Consort Road, London SW7 2AZ, UK*

Accepted 2021 March 19. Received 2021 March 17; in original form 2020 December 30

ABSTRACT

In this paper, we investigate whether overdensity formation via streaming instability is consistent with recent multiwavelength Atacama Large Millimeter Array (ALMA) observations in the Lupus star-forming region. We simulate the local action of streaming instability in 2D using the code ATHENA, and examine the radiative properties at mm wavelengths of the resulting clumpy dust distribution by focusing on two observable quantities: the optically thick fraction *ff* (in ALMA band 6) and the spectral index α (in bands 3–7). By comparing the simulated distribution in the *ff*–α plane before and after the action of streaming instability, we observe that clump formation causes *ff* to drop, because of the suppression of emission from grains that end up in optically thick clumps. α, instead, can either increase or decline after the action of streaming instability; we use a simple toy model to demonstrate that this behaviour depends on the sizes of the grains whose emission is suppressed by being incorporated in optically thick clumps. In particular, the sign of evolution of α depends on whether grains near the opacity maximum at a few tenths of a mm end up in clumps. By comparing the simulation distributions before/after clump formation to the data distribution, we note that the action of streaming instability drives simulations towards the area of the plane where the data are located. We furthermore demonstrate that this behaviour is replicated in integrated disc models provided that the instability is operative over a region of the disc that contributes significantly to the total mm flux.

Key words: accretion, accretion discs – hydrodynamics – instabilities – planets and satellites: formation – protoplanetary discs – circumstellar matter.

1 INTRODUCTION

According to core accretion theory, planets form through dust growth from initial μm-sized grains up to the size of a planet (Safronov & Zvjagina 1969). Since a substantial change in the grain mass and size is required in this process, different physical processes are expected to happen during dust growth; therefore, the process is often divided into three main stages (e.g. Lissauer 1993; Papaloizou & Terquem 2006; Armitage 2007): grain growth, where the dust grains grow from μm to cm, mainly through collision and sticking processes (Dominik & Tielens 1997; Birnstiel, Klahr & Ercolano 2012; Garaud et al. 2013; Dominik, Paszun & Borel 2016); planetesimal formation, from cm-sized dust grains to km-sized planetesimals; and protoplanet formation, which leads to spherical objects of $\sim 10^3$ km, which could be either rocky planets or gaseous planet cores (see e.g. Safronov & Zvjagina 1969; Kokubo & Ida 1996; Rafikov 2003; Ormel, Dullemond & Spaans 2010; Kobayashi, Tanaka & Okuzumi 2016; Kobayashi & Tanaka 2018).

The planetesimal formation stage represents a critical step in the growth process because the formation of km-sized objects is hampered by the so-called 'metre-sized barrier' or 'radial drift barrier' (Adachi, Hayashi & Nakazawa 1976; Weidenschilling 1977; Takeuchi & Lin 2002; Brauer, Dullemond & Henning 2008; Pinte & Laibe 2014). The aerodynamic interaction between dust and gas in protoplanetary discs, in fact, causes dust particles to lose angular momentum and to drift inwards. How rapidly the particles drift depends on the coupling between the gas and the dust, which is usually measured through the so-called Stokes number, τ_s. Since τ_s is proportional to the grain size, a, we can relate the radial drift to a, and it is possible to show that for grains characterized by $a \sim$ cm–m drift can be as fast as $t_{\rm drift} \sim 100$ yr at 1 au from the star (e.g. Armitage 2007; Birnstiel, Fang & Johansen 2016). Consequently, unless other mechanisms interfere with the inward drift, the ∼cm–m-sized grains are soon lost and they are no longer available to form planetesimals.

A potential way to avoid the metre-sized barrier is dust concentration in overdensities that rapidly collapse due to self-gravity (Johansen et al. 2007), and the streaming instability (Youdin & Goodman 2005) is a popular idea for how this might happen (Johansen & Youdin 2007; Youdin & Johansen 2007; Johansen et al. 2007). Like radial drift, the streaming instability is caused by the interaction between dust and gas components within the disc, and, more precisely, by the backreaction of dust on the gas. When exerted by partially coupled particles ($\tau_s \sim 1$), the dust backreaction is strong enough that it can locally trigger on the disc mid-plane a powerful hydrodynamic instability (the streaming instability; Youdin & Goodman 2005), which, in appropriate conditions, promotes fast particle clumping, forming dust overdensity regions (Youdin & Johansen 2007; Carrera, Johansen & Davies 2015; Yang, Johansen &

★ E-mail: ces204@cam.ac.uk

© 2021 The Author(s)
Published by Oxford University Press on behalf of Royal Astronomical Society

Downloaded from https://academic.oup.com/mnras/article/504/1/1495/6188383 by Imperial College London Library user on 25 June 2021

Carrera 2017). Thus, streaming instability might be the key to solving the planetesimal formation issue: on one hand, the formed clumps would interact in a different way with the gas and this would slow down the drift velocity; on the other hand, local overdensities would facilitate the gravitational collapse and then planetesimal formation (Johansen et al. 2007).

Clump formation through streaming instability can qualitatively be described as follows. The backreaction on the gas causes the gas component to orbit faster, and therefore it reduces the difference in azimuthal velocity between the gas and the dust; thus, the headwind on the particles becomes weaker (Youdin & Goodman 2005; Johansen & Youdin 2007; Squire & Hopkins 2020). If a dust overdensity were present, it would perturb the system equilibrium, causing a stronger backreaction, and therefore a reduced radial drift (which is determined by the difference in velocity between the two components). The system therefore faces an instability, as the initial dust overdensity increases more and more due to the new material drifting inwards from outer orbits and stopping in the clump (Johansen & Youdin 2007 described this effect as a 'traffic jam'); the consequence is an exponential growth of clumps, whose density can become as high as 10^3 times the gas density, ρ_g (e.g. Youdin & Johansen 2007; Bai & Stone 2010b,c). At the same time, some particles are lost from the inner radius of the clumps, due to radial drift; therefore, at some point a steady state is reached and the exponential growth saturates. The development of such exponentially growing instabilities is expected to be easier for marginally coupled particles (Johansen & Youdin 2007), because their backreaction is stronger (the fastest radial drift is expected to occur for $\tau_s \sim 1$).

The ability of streaming instability to form dust clumps depends on the local characteristics of the system, and in particular on the following three parameters: the grain Stokes number τ_s, which regulates the gas–dust interaction; the pressure support, Π, which gives rise to the relative velocity and thus ultimately generates the streaming instability; and the local dust-to-gas mass ratio, Z, which must exceed a certain threshold in order to create dust clumps. From the theoretical point of view, several studies focused on exploring this parameter space, in order to find which combinations of (τ_s, Π, Z) can trigger dust clumping via streaming instability. Bai & Stone (2010b,c) showed that, for a given grain size population, the stronger the pressure support, the higher is the critical Z to have streaming instability, whereas, for a given Z, smaller values of Π allow smaller particles to form clumps. More recently, Carrera et al. (2015) and Yang et al. (2017) studied in detail the critical Z required to trigger streaming instability for fixed τ_s (single grain population) and Π, identifying the regions of the Z–τ_s plane where streaming instability is expected to occur. Several studies also focused on the properties of streaming instability in multispecies simulations, both in the linear instability phase (Laibe & Price 2014; Drążkowska, Alibert & Moore 2016; Krapp et al. 2019; Zhu & Yang 2020) and in the non-linear phase (Bai & Stone 2010c; Schaffer, Yang & Johansen 2018). They found that, under certain conditions, the efficiency of linear growth can be increased/decreased when multiple grain species are considered with respect to the single grain models. As well as the physical properties of streaming instability, recent works studied in detail the influence of numerical parameters (size of the simulation box, resolution, etc.), algorithms, and boundary conditions on streaming instability simulations (Yang & Johansen 2014; Li, Youdin & Simon 2018).

From an observational perspective, the recent Disk Substructures at High Angular Resolution Project (DSHARP) survey (Andrews et al. 2018), conducted with the Atacama Large Millimeter Array (ALMA), provided high-resolution data for 20 protoplanetary discs, finding in most of them interesting substructures, such as rings, spirals, gaps, etc. These observations are allowing a more detailed analysis of the processes operating in protoplanetary discs, including planetesimal formation, thereby deepening our knowledge of these systems. Among other results, it has been found that the rings are marginally optically thick (Dullemond et al. 2018; Huang et al. 2018); this feature may be a mere coincidence, but it could also be the consequence of a common mechanism happening in rings, e.g. clump formation via streaming instability (Stammler et al. 2019).

Furthermore, Tazzari et al. (2020a,b) recently presented a new ALMA survey at 3 mm in Lupus star-forming regions. By combining these results to the previous surveys at 0.9 and 1.3 mm (Ansdell et al. 2016, 2018), they were able to study in detail the optical properties of observed systems and to extract important information about disc radii, the size–luminosity relation, the system optical depth, etc. Focusing on the spectral index and the optically thick fraction,[1] they noticed that the data concentrate in the region of spectral index ∼2.4–3 and with a range of values of the optically thick fraction, presenting a number of potential models that might explain the observed distribution in this plane.

In this context, the aim of this paper is to investigate whether the formation of optically thick substructures through the action of streaming instability is consistent with the observations by Tazzari et al. (2020a,b). We therefore simulate systems where streaming instability is present (taking advantage of the broad parameter analysis performed in the studies mentioned above) and analyse their optical properties after the formation of dust clumps. We then compute the two observable quantities considered by Tazzari et al. (2020a,b) – the optically thick fraction and the spectral index – in order to perform a comparison between the data and the final distribution from our simulations.

The paper is organized as follows: in Section 2, we briefly summarize the main parameters and equations describing streaming instability; in Section 3, we describe the simulations performed and the method applied to analyse their optical properties; Section 4 illustrates the process of clump formation in our simulations; the explanation of the consequences of the presence of substructures on optical properties is covered in Section 5, where we also introduce a toy model that mimics the action of streaming instability, and we compare the local results to the disc-averaged observations of Tazzari et al. (2020b); in Section 6, we define an integrated disc model and its optical properties are compared with the foregoing local results; finally, in Section 7 we discuss the influence of the main model parameters and grain composition on the final results.

2 DUST–GAS INTERACTION AND STREAMING INSTABILITY

Protoplanetary discs contain both dusty and gaseous materials, in an overall initial dust-to-gas ratio of about 1:100. Both the components orbit around the central star, but their azimuthal velocities v_ϕ are moderately different between each other; in fact, v_ϕ is the result of the balance of gravitational, pressure, and centrifugal forces in the case of gas, whereas the dust is subject only to gravity and centrifugal force, and the absence of pressure force makes the dust azimuthal velocity slightly faster than that of the gas. This results in an aerodynamic interaction between the two components, exerted through drag forces,

[1]Defined as the ratio of the flux to that of an optically thick disc of the same size; see Section 3.4.

Downloaded from https://academic.oup.com/mnras/article/504/1/1495/6188383 by Imperial College London Library user on 25 June 2021

which (together with the consequent backreaction) plays the main role in triggering the streaming instability.

In this paper, we consider the Epstein drag force (valid for particles smaller than their main free path; Epstein 1924):

$$F_{\rm D} = \frac{4\pi}{3}\rho_{\rm g} a^2 v v_{\rm th}, \tag{1}$$

where a is the particle radius, $\rho_{\rm g}$ is the gas density, and $v_{\rm th}$ is the gas thermal velocity. The ratio between the particle momentum and the drag force provides the interaction time-scale between the gas and the dust grains of different sizes

$$t_{\rm s} = \sqrt{\frac{\pi}{8}}\frac{\rho_{\rm p} a}{\rho_{\rm g} v_{\rm th}}, \tag{2}$$

which can be conveniently expressed in units of the dynamical time-scale Ω^{-1}

$$\tau_{\rm s} = t_{\rm s}\Omega, \tag{3}$$

obtaining the dimensionless stopping time, usually called Stokes number, which provides information about the coupling between gas and dust: $\tau_{\rm s} \ll 1$ means that the time-scale for interaction is significantly smaller than the dynamical time; thus, the particles, at first approximation, follow the gas motion; on the contrary, if $\tau_{\rm s} \gg 1$, the dust–gas coupling is weak and the particle motion is barely affected by the gas.

Equation (3) can also be reversed to compute the grain size corresponding to a given Stokes number

$$a = \frac{2}{\pi}\frac{\tau_{\rm s}\Sigma_{\rm g}}{\rho_{\rm p}}, \tag{4}$$

where $v_{\rm th}$ is written in terms of the isothermal sound speed $c_{\rm s} \sim \Omega_{\rm k} H_{\rm g}$, and $\rho_{\rm g} = \rho_0 \exp[-z^2/(2H_{\rm g}^2)] = \Sigma_{\rm g}/(\sqrt{2\pi}H_{\rm g})$ is the Gaussian profile assumed for the gas density ($\Sigma_{\rm g}$ is the vertically integrated gas density).

The pressure gradient, which is the main cause of drag between dust and gas, is often characterized by the so-called pressure support parameter, defined as

$$\Pi = \eta\frac{v_{\rm k}}{c_{\rm s}} = \eta\left(\frac{H_{\rm g}}{R}\right)^{-1}, \tag{5}$$

where $H_{\rm g}$ is the gas scale height, $v_{\rm k}$ is the Keplerian velocity, $c_{\rm s}$ is the sound speed, and η is related to the pressure gradient

$$\eta = \frac{1}{2}\left(\frac{H_{\rm g}}{R}\right)^2\frac{\partial \log P}{\partial \log R}. \tag{6}$$

Finally, we introduce the dust-to-gas ratio (also called metallicity), defined as the ratio between the dust and gas densities ($\Sigma_{\rm d}$ and $\Sigma_{\rm g}$, respectively), as follows:

$$Z = \frac{\Sigma_{\rm d}}{\Sigma_{\rm g}}, \tag{7}$$

which is required to be high in order to trigger streaming instability. Note that the requirement of high Z is just a local requirement; thus, it is not in tension with the fact that the global dust-to-gas ratio is of the order of 1:100.

Bai & Stone (2010a) implemented in ATHENA the dust–gas equations, written in a local reference frame located at a fixed radius R_0 and rotating at angular velocity Ω (non-inertial reference frame). The continuity equation for the gas is

$$\frac{\partial \rho_{\rm g}}{\partial t} + \nabla \rho_{\rm g}\mathbf{u}_{\rm g} = 0, \tag{8}$$

where $\rho_{\rm g}$ and $\mathbf{u}_{\rm g}$ are the gas density and velocity, respectively; the Euler equation for the gas is

$$\frac{\partial \rho_{\rm g}\mathbf{u}_{\rm g}}{\partial t} + \nabla\left(\rho_{\rm g}\mathbf{u}_{\rm g}\mathbf{u}_{\rm g} + P\mathbf{I}\right) = \rho_{\rm g}\left(2\mathbf{u}_{\rm g}\times\mathbf{\Omega} + 3\mathbf{\Omega}^2 x\hat{\mathbf{x}} - \mathbf{\Omega}^2 z\hat{\mathbf{z}} + \sum_k \epsilon_k \frac{\mathbf{v_k} - \mathbf{u}_{\rm g}}{t_{{\rm s},k}}\right), \tag{9}$$

where P is the pressure, ϵ_k is the dust-to-gas ratio (for particle species k), $t_{{\rm s},k}$ is the stopping time of k particle species, and σ_k and $\mathbf{v_k}$ are the particle local mass density and velocity, respectively. The left-hand side includes the momentum time derivative and the effects due to advection and pressure gradient; the right-hand side includes the action of Coriolis force (first term), radial tidal momentum (second term), vertical gravity (third term), and backreaction (fourth term). The i-particle equation of motion is

$$\frac{{\rm d}\mathbf{v_i}}{{\rm d}t} = -2\eta v_{\rm k}\mathbf{\Omega}\hat{\mathbf{x}} + 2\mathbf{v_i}\times\mathbf{\Omega} + 3\mathbf{\Omega}^2 x_i\hat{x} - \mathbf{\Omega}^2 z_i\hat{z} - \frac{\mathbf{v_i} - \mathbf{u}_{\rm g}}{t_{{\rm s},k}}, \tag{10}$$

where the first term on the right-hand side is the effect of the pressure gradient, and all the other terms correspond to those in equation (9).

We have neglected the self-gravity of the dust in these simulations. Since, as we show later, the clumps formed in our simulations without self-gravity already contribute negligibly to the total flux of the disc, the inclusion of self-gravity, which acts to further enhance clumping, is not expected to have a significant effect on the observed properties.

We also neglected the effects of turbulence, as is common in streaming instability simulations (Liu & Ji 2020). Turbulence is generally expected to reduce particle clumping via streaming instability (Gole et al. 2020; Umurhan, Estrada & Cuzzi 2020); therefore, the usual no-turbulence assumption corresponds to the most optimistic case for clumping via streaming instability.

3 METHODS

To understand whether the action of streaming instability is consistent with recent ALMA observations, we characterize the system observable quantities before and after the action of streaming instability. Our method can be described as a four-step process: (1) We perform hydrodynamics simulations of systems where streaming instability takes place; (2) we define a physical disc model, which allows us to translate the simulation results to physical systems; (3) we compute the radiative properties of these systems; and (4) we compare two observable properties to those derived from ALMA observations by Tazzari et al. (2020a,b).

3.1 Numerical simulations

To simulate the action of streaming instability, we perform 2D hydrodynamics simulations of dust and gas using the hybrid code ATHENA, which treats the gas as a fluid on a Eulerian grid (Stone et al. 2008) and the dust as superparticles on that grid (Bai & Stone 2010a). We use a 2D (vertical and radial directions) shearing box approach, which allows us to simulate a portion of the disc located at an arbitrary radius R_0 and rotating at angular velocity $\Omega_{\rm k}(R_0)$.

In the following, the simulation parameters are given in code units: The time unit is the dynamical time $\Omega_{\rm k}^{-1}$ and the length unit is the gas layer thickness $H_{\rm g}$. The choice of the mass unit is arbitrary, because the equations describing gas and dust interaction (equations 9 and 10) depend on the dust-to-gas mass ratio, but are independent of the disc mass.

For all the 12 simulations we performed, we considered a box of size $L_r \times L_z = 0.05 \times 0.15$ (L_r and L_z are the radial and vertical

Downloaded from https://academic.oup.com/mnras/article/504/1/1495/6188383 by Imperial College London Library user on 25 June 2021

Table 1. Parameters of the simulations.

Name	τ_s^{min}	τ_s^{max}	Π	Z	q
T41-Z02-Q3	10^{-4}	10^{-1}	0.025	0.02	3
T41-Z02-Q35	10^{-4}	10^{-1}	0.025	0.02	3.5
T41-Z02-Q4	10^{-4}	10^{-1}	0.025	0.02	4
T41-Z03-Q3	10^{-4}	10^{-1}	0.025	0.03	3
T41-Z03-Q35	10^{-4}	10^{-1}	0.025	0.03	3.5
T41-Z03-Q4	10^{-4}	10^{-1}	0.025	0.03	4
T30-Z02-Q3	10^{-3}	1	0.025	0.02	3
T30-Z02-Q35	10^{-3}	1	0.025	0.02	3.5
T30-Z02-Q4	10^{-3}	1	0.025	0.02	4
T30-Z03-Q3	10^{-3}	1	0.025	0.03	3
T30-Z03-Q35	10^{-3}	1	0.025	0.03	3.5

box lengths, respectively), split into $N_r \times N_z = 256 \times 768$ cells. In each box, we include $N_{tot} = 7 \times 10^5$ particles, equally distributed in $N_{species} = 28$ particle species. The Stokes numbers of the different species are uniformly distributed in log space between minimum and maximum Stokes numbers, τ_{min} and τ_{max}, respectively; six of our simulations are characterized by $\tau_{min} - \tau_{max} = (10^{-4})$–$(10^{-1})$, and six are characterized by $\tau_{min} - \tau_{max} = (10^{-3})$–(1). The pressure support parameter is $\Pi = 0.025$ in all the simulations, while two values for the dust-to-gas mass ratio are considered ($Z = 0.02$ and 0.03).

All the simulations evolve for at least 1500 dynamical times, in some cases simulations had not reached a steady state in $1500\,\Omega^{-1}$; thus, the running time has been extended to $2000\,\Omega^{-1}$ (see Appendix A for more details).

We use reflecting boundary conditions in the vertical direction and periodic boundary conditions in the radial direction.

As initial conditions, all the particle species are distributed according to a Gaussian-shaped distribution in the vertical direction, centred in the disc mid-plane, whose standard deviation (corresponding to the initial layer thickness) is $H_d = 0.015 H_g$. We use the parameter q to specify the particle mass distribution per logarithmic particle radius bin

$$\frac{dM_p}{d\log a} \propto a^{4-q}, \tag{11}$$

or, equivalently, the number distribution $n(a)$

$$n(a) = \frac{dN_p}{da} = n_0 a^{-q}, \tag{12}$$

where M_p and N_p are the particle mass and number, respectively. In our simulations, we consider $q = 3$, 3.5, and 4 for each choice of Z and set of Stokes numbers.

In Table 1, we summarize the parameter used in our simulations.

3.2 Physical model

Studying the optical properties of simulated systems requires the definition of a disc model, allowing conversion of the dimensionless simulation results into physical units. As reference model, we consider the Minimum Mass Solar Nebula model by Chiang & Youdin (2010).

Chiang & Youdin (2010) model is characterized by a flaring index $f = 2/7$; thus, the aspect ratio at the generic disc radius R is

$$H_g(R) = H_g(R_0) R \left(\frac{R}{R_0}\right)^{2/7}, \tag{13}$$

where R_0 is the box location (in the following, we take $R_0 = 35$ au, unless otherwise specified) and the aspect ratio at R_0 corresponds to the length unit $L_{unit} = H_g(R_0)$.

The time unit is defined as the inverse Keplerian velocity at the box location $t_{unit} = \Omega_k^{-1}(R_0)$. Thus, it depends only on the box location and the star mass, which we assume to be the same as that of the Sun $M_* = M_\odot$.

We then choose the arbitrary mass unit by fixing the gas density at 1 au and computing the gas density at box location R_0 as

$$\Sigma_g(R_0) = \Sigma_g(1\,\text{au}) \left(\frac{R_0}{\text{au}}\right)^{-p}, \tag{14}$$

where $p = 1.5$ in Chiang & Youdin (2010) model. We do not fix a single value for the gas density, but we vary it in the range $\Sigma_g(1\,\text{au}) = 100$–$3000\,\text{g cm}^{-2}$ [cf. $2200\,\text{g cm}^{-2}$ in Chiang & Youdin (2010) model], which corresponds to $\Sigma_g(R_0) = 0.5$–$14.5\,\text{g cm}^{-2}$; for each simulation, therefore, we obtain a population of discs characterized by different masses. For a disc characterized by inner and outer radii $R_{in} = 0.1$ and 70 au, respectively, the chosen density distribution corresponds to discs of masses between 10^{-3} and $3 \times 10^{-2}\,M_\odot$.

Finally, we define the temperature profile

$$T(R) = T_0 \left(\frac{R}{\text{au}}\right)^{-3/7} \left(\frac{L_*}{L_\odot}\right)^{1/4}, \tag{15}$$

where the temperature at 1 au is $T_0 = 120$ K (unless stated otherwise) and the temperature profile is the same as that used in the review by Chiang & Youdin (2010), while the star luminosity is $L_* = L_\odot$. The corresponding temperature at the box location (35 au) for the chosen temperature profile is $T(R_0) \sim 26$ K.

3.3 Optical properties

To study the dust optical properties, we start by computing the opacity of dust grains; we use Birnstiel et al. (2018) dust code (which applies the Mie theory combined with optical data sets to compute the system optical properties), assuming (similarly to Tazzari et al. 2016) spherical compact grains, whose composition includes water, silicates (from Warren & Brandt 2008; Draine 2003), troilite (from Henning & Stognienko 1996), and organics (from Zubko et al. 1996). Note that the chosen composition is similar to that labelled as 'Zubko' in Birnstiel et al. (2018).[2]

Through Birnstiel et al. (2018) code, we obtain the dust material density $\rho_p = 1.632\,\text{g cm}^{-3}$, used to compute the dust grain size

$$a = \frac{2}{\pi} \frac{\Sigma_g \tau_s}{\rho_p}. \tag{16}$$

Then, we extract from Birnstiel et al. (2018) code the opacity corresponding to each simulated grain size and selected wavelength, obtaining the single grain opacity $k_\nu^{single}(a)$.

Since the real grain size distribution is expected to be continuous, each simulated a_i represents a set of grain sizes between a_i and $a_i + da_i$; thus, we compute the opacity of each grain size as the average opacity

$$k_\nu^{abs}(a_i) = \frac{\int_{a_i - da_i}^{a_i} k_\nu^{single}(a) m(a) n(a) da}{\int_{a_i - da_i}^{a_i} m(a) n(a) da}. \tag{17}$$

[2]See Section 7.3 for a discussion on the composition choice.

Downloaded from https://academic.oup.com/mnras/article/504/1/1495/6188383 by Imperial College London Library user on 25 June 2021

Then, we compute the size averaged opacity, which gives the system average response (see the Appendix B for further details)

$$k_\nu^{\rm avg} = \frac{\int_{a_{\rm min}}^{a_{\rm max}} k_\nu^{\rm abs}(a) m(a) n(a) {\rm d}a}{\int_{a_{\rm min}}^{a_{\rm max}} m(a) n(a) {\rm d}a}, \tag{18}$$

where $m(a)$ is the mass of the dust grain. The main characteristics of $k_\nu^{\rm avg}$ as a function of the maximum grain size $a_{\rm max}$ are the presence of a steep increase when $a_{\rm max} \sim \lambda/(2\pi)$, followed by a decline towards larger $a_{\rm max}$ values.

We use the information on $k_\nu^{\rm avg}$ to obtain the optical depth

$$\tau_\nu = \frac{k_\nu^{\rm avg} \Sigma_{\rm d}}{\cos i}, \tag{19}$$

where we assume the inclination angle to be $i = 0$, and we use this information to obtain the specific intensity (assuming that the system is in local thermodynamical equilibrium)

$$I_\nu = B_\nu(T)(1 - {\rm e}^{-\tau_\nu}), \tag{20}$$

where B_ν is the Planck function evaluated at the local temperature $T(R)$ [for the location of the considered box we obtain $T(R_0) \sim$ 26 K]. Finally, we compute the flux

$$F_\nu \propto \int I_\nu {\rm d}A. \tag{21}$$

3.4 Comparison with observations

After studying the systems' optical properties, we compare our simulations to the observations obtained by Tazzari et al. (2020a,b) in the Lupus star-forming region. Therefore, we focus on the same plane used in Tazzari et al. (2020a,b) to study their data distribution: the optically thick fraction − spectral index plane.

The optically thick fraction is defined as the ratio between the system flux F_ν and the flux that the system would emit if it was a blackbody

$$ff = \frac{F_\nu}{F_{\nu,\rm blackbody}} = \frac{\int I_\nu {\rm d}A}{\int B_\nu {\rm d}A}, \tag{22}$$

where B_ν is the Planck function. Note that if a system were optically thick ($\tau_\nu \gg 1$), it would have $I_\nu \sim B_\nu$ (see equation 20) and therefore $ff \sim 1$; on the contrary, an optically thin system ($\tau_\nu \ll 1$) would be characterized by $I_\nu \sim \tau_\nu B_\nu$, thus $ff \sim \tau_\nu$.

The spectral index, instead, measures the frequency dependence of the flux

$$\alpha = \frac{\partial \log F_\nu}{\partial \log \nu}. \tag{23}$$

It is also useful to introduce the opacity index (see Appendix B for further information)

$$\beta = \frac{\partial \log k_\nu^{\rm avg}}{\partial \log \nu}, \tag{24}$$

which describes the variation of the opacity with frequency (assuming that $k_\nu^{\rm avg} \propto \nu^\beta$). $\beta(a_{\rm max})$ describes how $k_\nu^{\rm avg}$ varies with $a_{\rm max}$; we thus expect β to have a peak for $a_{\rm max} \sim \lambda/(2\pi)$, i.e. where $k_\nu^{\rm avg}$ has a steep increase with grain size. Since the value of $a_{\rm max}$ corresponding to peak opacity scales with the wavelength, if we consider any two wavelengths λ_1 and λ_2, so that $\lambda_1/(2\pi) < a_{\rm max} < \lambda_2/(2\pi)$, the opacity is much higher at wavelength λ_1 and hence the value of beta is large (see Appendix B for further details and plot regarding the spike in β).

In the limit of low optical depth $F_\nu \propto \tau_\nu B_\nu$, α can be related to the opacity index β:

$$\alpha = \frac{\partial \log B_\nu}{\partial \log \nu} + \beta, \tag{25}$$

which can be derived by using equations (23) and (24). In the Rayleigh–Jeans limit, $\alpha = 2 + \beta$. Thus, higher α is associated with higher β in the optically thin case; for optically thick emission in the Rayleigh–Jeans limit, $\alpha = 2$.

We populate the *ff*–α plane with the simulation results and, by adding on the same plane the data distribution by Tazzari et al. (2020a,b), we verify whether or not the simulations are consistent with observations. Since the data are available in ALMA bands 3 (100 GHz, 3.3 mm), 6 (230 GHz, 1.33 mm), and 7 (345 GHz, 0.88 mm), we compute the optical properties in these bands; specifically, we compute the optically thick fraction in band 6 $ff_{\rm B6}$, while we use band 3 and band 7 to compute the spectral index $\alpha_{\rm B3\text{-}B7}$ (note that we need two values to compute α, because it is defined as a derivative).

4 CLUMP FORMATION VIA STREAMING INSTABILITY

Considering, as an example, simulation T41-Z03-Q4 (see Table 1) in this section we study the properties of clumps formed in the simulated box due to the action of streaming instability.

In Fig. 1, we show the vertically integrated density profiles of dust [$\sigma_{\rm dust}(R, z)$ is the 2D dust density, in vertical and radial directions]:

$$\Sigma_{\rm dust}(R) = \int_{-L_z/2}^{L_z/2} \sigma_{\rm dust}(R, z) {\rm d}z, \tag{26}$$

for a selection of 10 particle species from the 28 species used in the simulation. The three panels correspond to different time-steps of the system evolution: $t = 0\,\Omega^{-1}$ (left-hand panel), $t = 200\,\Omega^{-1}$ (central panel), and $t = 2000\,\Omega^{-1}$ (right-hand panel). The density profile of each particle species corresponds to a different colour in a rainbow palette, from the smallest particle species in red to the biggest one in magenta.[3]

The initial density profiles (left-hand panel) are uniform for all the particle species, and clumps are gradually formed as the system evolves (central and right-hand panels). By comparing the central and right-hand panels, we notice that the biggest particle species (magenta, violet, and blue lines) are already involved in clumps after 200 Ω^{-1}, while smaller species (cyan and green lines) require more time to participate in clumps; the smallest particle species (yellow and orange lines), instead, never participate in clumping. In fact, particles characterized by Stokes number close to 1 are the most affected by the drag forces, thus they are expected to clump via streaming instability more rapidly, while the smallest particles are highly coupled to the gas, thus they follow gas evolution and do not clump.

5 IMPACT OF STREAMING INSTABILITY ON OBSERVATIONS: LOCAL MODEL

In this section, we study the observable properties of the simulated boxes undergoing streaming instability. In the following, unless

[3]Given the very small area occupied by the clumps at the end of the simulation, they are expected to contribute negligibly to the disc total flux; thus (as anticipated in the previous section), the inclusion of self-gravity is not expected to affect significantly the observable properties.

Downloaded from https://academic.oup.com/mnras/article/504/1/1495/6188383 by Imperial College London Library user on 25 June 2021

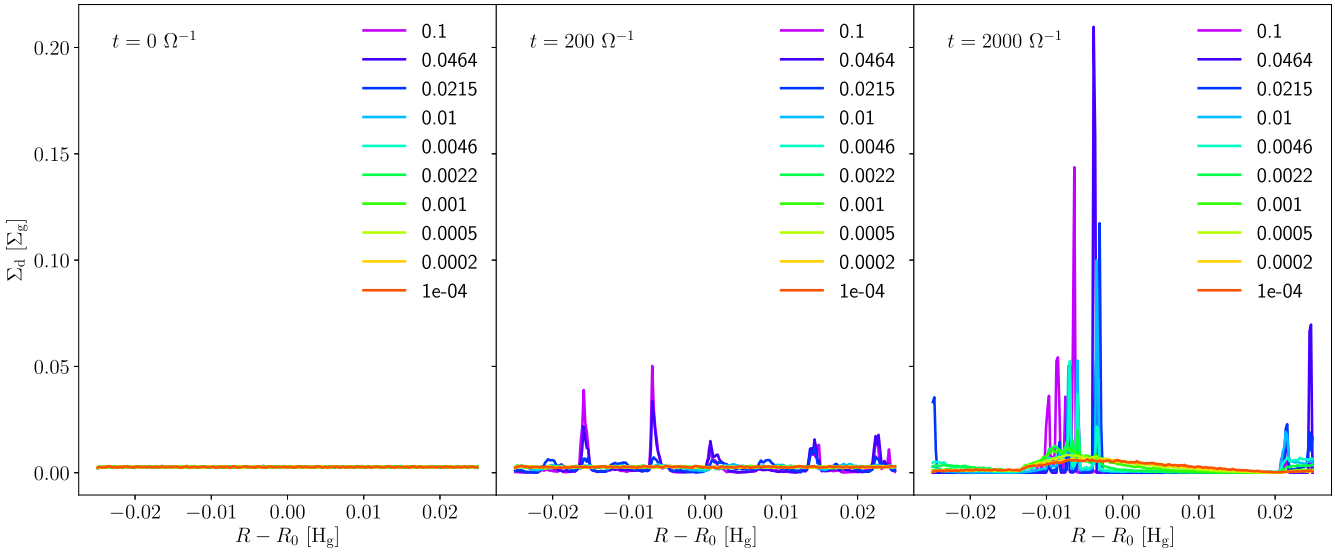

Figure 1. Dust radial density profiles as a function of radius in the simulated box for simulation T41-Z03-Q4. The rainbow colour palette goes from red, which corresponds to the smallest particle species, to magenta, which corresponds to the biggest particle species. The three plots correspond to three different simulation time-steps: the initial condition $t = 0\ \Omega^{-1}$ (left-hand panel), when all the particle species have a uniform density $\Sigma_d \sim 0.003$; an intermediate snapshot $t = 200\ \Omega^{-1}$ (central panel); and the result at the end of the simulation $t = 2000\ \Omega^{-1}$ (right-hand panel).

specified otherwise, we adopt the disc physical model described in Section 3.2.

5.1 Distribution in the *ff*–α plane before and after particle clumping

To analyse the effects on the optical properties caused by clump formation via streaming instability, we examine the optically thick fraction (equation 22) and the spectral index (equation 23) of the integrated emission from the box, both before and after the formation of clumps. Since the simulations are scale free (being characterized by the dimensionless numbers set out in Table 1), we can map a single simulation on to a variety of outcomes through considering a range of gas surface densities in the box; we considered 10 values for Σ_g at the box location, logarithmically distributed between 0.5 and 14.5 g cm^{-2}.

In Fig. 2, we show the distribution in the *ff*–α plane for three simulations (T41-Z03-Q4, T30-Z02-Q4, and T30-Z03-Q3; see Table 1). In all the three panels, the blue squares represent the initial distribution of the selected systems, whereas the magenta diamonds correspond to the distribution of the 10 discs at the end of the simulation, i.e. after clumps have formed. The black arrows link together the initial and final conditions of the same system. The intensity of the blue/magenta symbols indicates the gas surface density, with the darkest (lightest) shading indicating the highest (lowest) surface density values. For reference, the data distribution is shown in the same plane with the green stars; we notice that clump formation either drives the models towards the area occupied by the data (left-hand panel), or keeps the models in the data area (central panel), or does not affect significantly the distribution (right-hand panel). See Sections 5.2 and 6 for a detailed comparison between simulations and data.

Focusing first on the initial conditions (blue squares), we notice that even if they are different in the three considered simulations (due to the difference in the parameter choices), they show some common features. In all cases, the system characterized by the highest gas surface density (darkest blue square) represents the highest value for *ff* and the lowest one for α: At fixed metallicity, this system has the highest dust surface density and hence optical depth and the value of α is therefore close to 2 as expected for optically thick emission. Conversely, for lower gas surface density, the lower optical depth results in systems with lower *ff* and higher α.

We consider first the evolution of *ff* when clumps form. Clumping involves depositing some of the grains in regions where the optical depth is higher than it was initially; if the clumps are optically thin, then this does not affect the overall flux produced by the box. However, if the clumps are optically thick then it means that some of the emission from grains in the uniform initial conditions is now hidden and therefore the overall flux declines. Consequently, clumping in general reduces *ff*, though in the case of very optically thin initial conditions (as in the right-hand panel where the high maximum Stokes number and relatively low q mean that the emission is dominated by large, low-opacity grains) *ff* may be hardly affected by clumping.

The effect on α is subtler and depends on the grain size (and hence optical properties) of the grains that are removed from the uniform background and deposited in optically thick clumps where their emission is concealed. Recalling that it is the largest grains that are deposited in the clumps, the direction of evolution of α depends on whether these largest grains have higher or lower opacity index, β, than the rest of the grain population.

We illustrate this effect via a 'toy model' (see also Appendix C for more details) in which we modify the initial conditions of a system to mimic clump formation by modifying the particles' distribution. Since in Section 4 we observed that only particle species characterized by high Stokes numbers participate in clumping, we split the grains into two groups: half of the grains (the smallest ones) are left in the uniform background, whereas the density profile of the remaining grains (the biggest ones) is modified as follows:

$$\Sigma_{j,i}(R) = \begin{cases} \frac{\Sigma_{j,0}}{p_i} & R_0 - \mathrm{d}R_i/2 < R < R_0 + \mathrm{d}R_i/2,\ j \geq 15 \\ 0 & \text{otherwise} \end{cases} \quad (27)$$

where j indicates the j-th species; $\Sigma_{j,0}$ is the initial uniform density and $\mathrm{d}R_i$ represents the radial fraction of the 2D box in which we

Downloaded from https://academic.oup.com/mnras/article/504/1/1495/6188383 by Imperial College London Library user on 25 June 2021

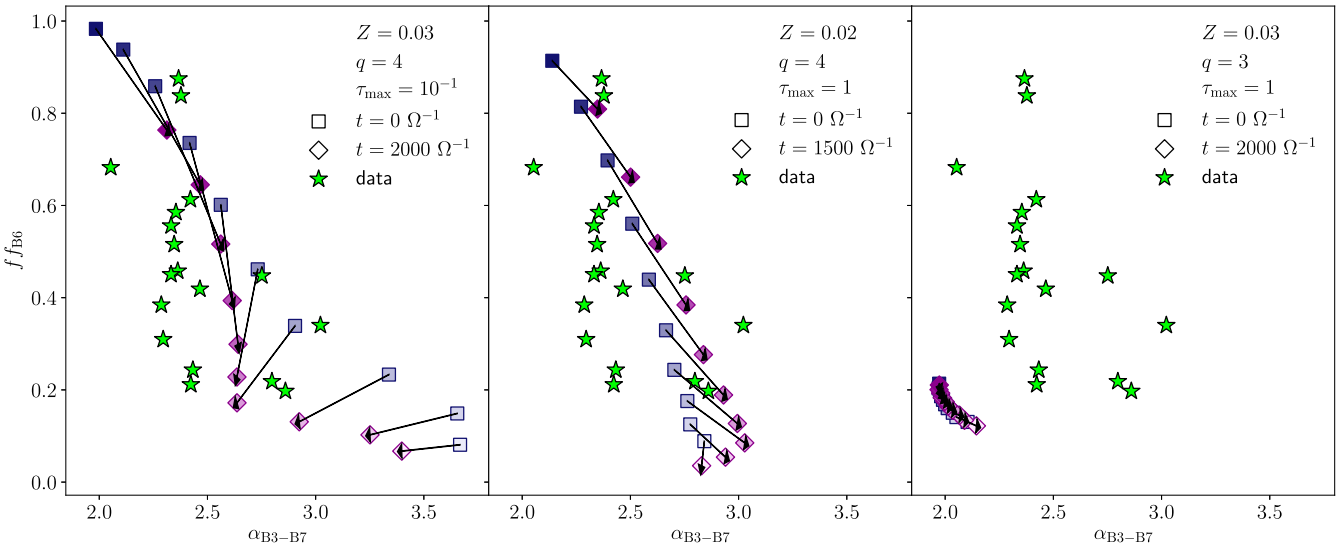

Figure 2. Distribution in the *ff*–α plane of simulations T41-Z03-Q4 (left-hand panel), T30-Z02-Q4 (central panel), T30-Z03-Q3 (right-hand panel). The blue squares correspond to the distribution for the systems initial conditions, while the magenta diamonds correspond to the distribution at the end of the system evolution; the arrows link the initial *ff*–α values to the corresponding ones at the end of the simulation. The shades of colours correspond to different gas densities: from the highest density [$\Sigma_{\rm g}(R_0) = 14.5\ {\rm g\,cm^{-2}}$, corresponding to $M_{\rm disc} \sim 3 \times 10^{-2}\ {\rm M_\odot}$], represented by the darkest blue/magenta markers, to the lowest density [$\Sigma_{\rm g}(R_0) = 0.5\ {\rm g\,cm^{-2}}$, corresponding to $M_{\rm disc} \sim 10^{-3}\ {\rm M_\odot}$], represented by the lightest blue/magenta markers. The green stars illustrate the data distribution by Tazzari et al. (2020a).

concentrate the dust

$$\mathrm{d}R_i = p_i(R_{\max} - R_{\min}), \tag{28}$$

where $p_i \in [0, 1]$. Note that we are redistributing only the biggest particles; thus, $\Sigma_{\rm d}$ will not be 0 outside the main peak, since the smallest particles are retained in the background; thus, the total dust density for each clump model i is given by

$$\Sigma_{\rm d,i}(R) = \sum_{j\leq 14} \Sigma_{j,0}(R) + \sum_{j\geq 15} \Sigma_{j,i}(R). \tag{29}$$

In the left-hand panel of Fig. 3, we show the dust density profiles obtained by redistributing the initial uniform dust density (black line) of simulation T30-Z03-Q4, considering $\Sigma_g = 0.5\ {\rm g\,cm^{-2}}$ and 11 values for parameter p_i, logarithmically distributed between 0.01 and 1 (the clump height increases from the lowest value in black to the highest value in pale pink).

In the right-hand panel of Fig. 3, we show the distribution in the *ff*–α plane (as before, we consider $\Sigma_{\rm g} = 0.5$–$14.5\ {\rm g\,cm^{-2}}$) obtained by computing the observable quantities for each clump width: The colours in this plot correspond to the dust distribution on the left with the same colour, while the black arrows link together the initial and final conditions of the same system. To explain the behaviour of the spectral index, we focus on the lowest density model (lower right in the plot) and the highest density model (upper left in the plot), which show opposite behaviours in α.

We first recall that the spectral index (in the optically thin limit) can be related to the opacity index as follows:

$$\alpha \sim \frac{\partial \log B_\nu}{\partial \log \nu} + \beta; \tag{30}$$

thus, we expect α to increase (decrease) when β increases (decreases). We therefore show in Fig. 4 the opacity index β as a function of the maximum grain size $a_{\max}$ (black line). The two panels correspond to the highest and lowest density models on the left and right, respectively. In both the panels, two coloured areas highlight the β corresponding to clumping (intense violet/blue area) and non-clumping (light blue/violet area) particle species in the simulation (separated at a Stokes number of $\tau_{\rm s} = 0.036$, which corresponds to different grain sizes in the two panels).

We notice that, in the lowest density case, the clumping grains are close to the opacity resonance and hence have higher β values than the rest of the population. Once these grains go into the clumps (which are optically thicker than the uniform background), their contribution to the system's emission is downweighted. Therefore, the overall β decreases and thus we expect α to decrease – as, indeed, happens in the lowest density model in the right-hand panel of Fig. 3. On the contrary, when we consider the opacity index for the highest density model (right-hand panel in Fig. 4), we observe that clumping species are here characterized by lower β values than the non-clumping species. Thus, we expect both β and α to increase after particle clumping, which is consistent with the behaviour of the highest density model in the right-hand panel of Fig. 3.

These behaviours can be related to Fig. 2.[4] In the central panel, the high maximum Stokes number implies relatively large grains and hence clumping increases the spectral index (though this effect is weaker at the lowest gas surface densities where the grain size is smaller at fixed Stokes number). In the left-hand panel, conversely, the lower maximum Stokes number places the largest grains in the simulation close to the opacity resonance. Clumping therefore reduces α in this case.

5.2 Comparison with data

In Fig. 5, we show the distributions in the *ff*–α plane for all the simulated systems and for the data distribution (green stars) obtained by Tazzari et al. (2020a,b).

[4]Note that if the clumping factors p for each species are computed from the simulation, then the toy model is able to recover the precise behaviour of simulations (see Appendix C).

Downloaded from https://academic.oup.com/mnras/article/504/1/1495/6188383 by Imperial College London Library user on 25 June 2021

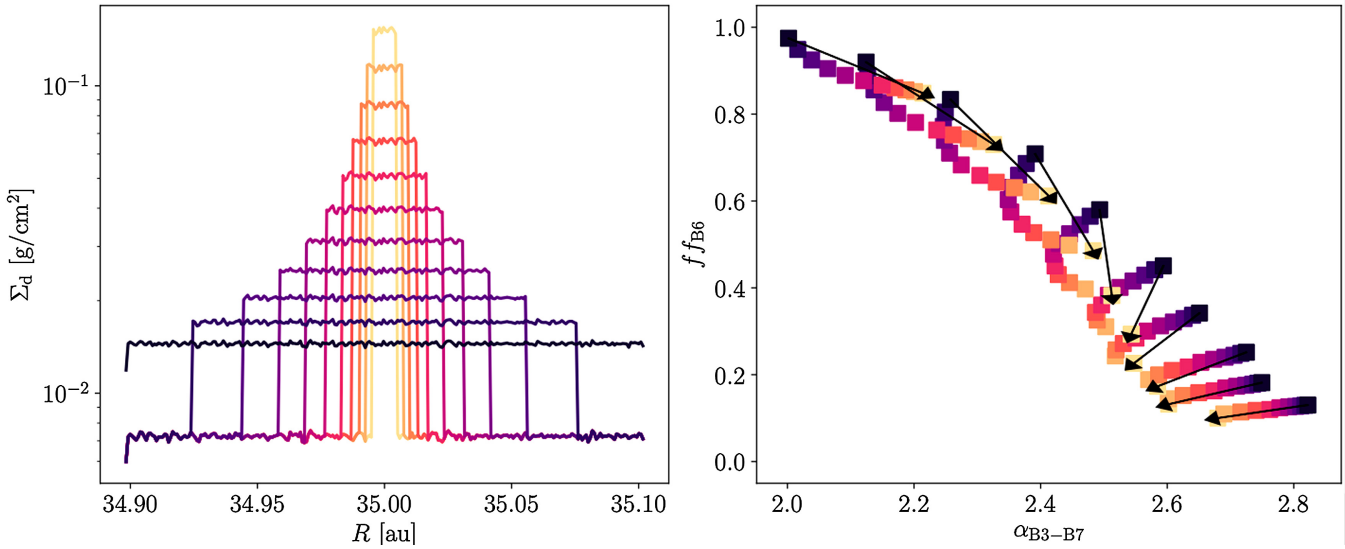

Figure 3. Left-hand panel: redistribution of the initial homogeneous dust density of simulation T30-Z03-Q4 (for the case with local gas density $\Sigma_g = 0.5\,\mathrm{g\,cm^{-2}}$) to create artificial clumps characterized by various heights and widths, assuming that only half of the particle species clump (the biggest ones); a colour code is used, so that dust concentration increases moving from black to pale pink. Right-hand panel: observable quantities for all the density distributions considered in the left-hand panel (the colour of each square indicates at which dust density redistribution that colour corresponds) and different values of Σ_g.

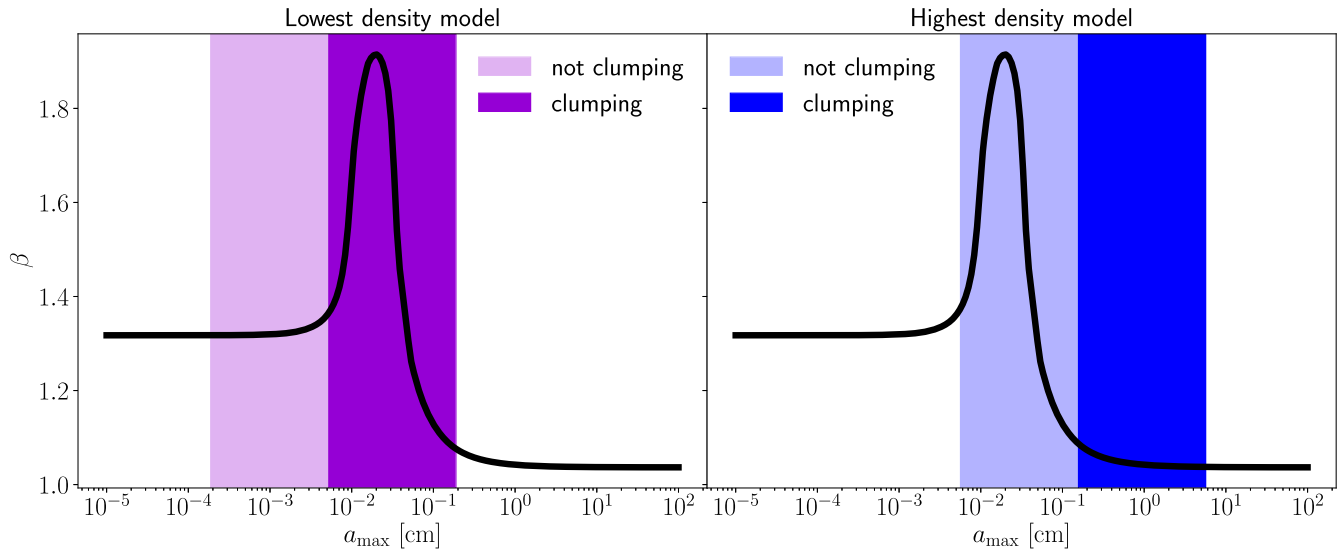

Figure 4. Both panels: opacity index as a function of the grain size obtained using Birnstiel et al. (2018) code (black line); the intense violet/blue area highlights the values of β corresponding to the clumping species sizes in the toy model, while the light violet/blue area highlights the values of β corresponding to the non-clumping species sizes. The plot in the left-hand panel is obtained considering the lowest density model in this paper ($\Sigma_g = 0.5\,\mathrm{g\,cm^{-2}}$), while the plot in the right-hand panel is obtained considering the highest density model in this paper ($\Sigma_g = 14.5\,\mathrm{g\,cm^{-2}}$). Note that grain size distribution is assumed to be a power law with $q = 4$.

We split the simulations into two groups characterized by the same Stokes number range: In the left-hand panels, we show the initial (upper panel) and final (lower panel) distributions for simulations characterized by $\tau_s = (10^{-4})$–(10^{-1}); the right-hand panels show the initial (upper panel) and final (lower panel) distribution for simulations characterized by $\tau_s = 10^{-3}$–1. In each panel, the different colours refer to different combinations of q and Z, as indicated in the plot legend.

It is worth noticing that the initial distributions (upper panels) partially cover the data distribution. However, most cases characterized by $\tau_{max} = 10^{-1}$ have too high optically thick fractions in the highest density models, which are unable to cover the lower left area where data lie; secondly, the lowest density models present too high values for α. Similarly, some of the $\tau_{max} = 1$ models present *ff* higher than those of the data (see, in particular, the yellow and pink models).

If we then compare the initial distributions to the final ones (lower panels), we note that the action of streaming instability pushes the simulated systems into the region occupied by data. Indeed, the optically thick fraction is lowered by clump formation, and this effect enables the high density models to re-cover the low-*ff* data that previously were not matched by simulations. Moreover, the spectral index of the low density models is significantly reduced

Downloaded from https://academic.oup.com/mnras/article/504/1/1495/6188383 by Imperial College London Library user on 25 June 2021

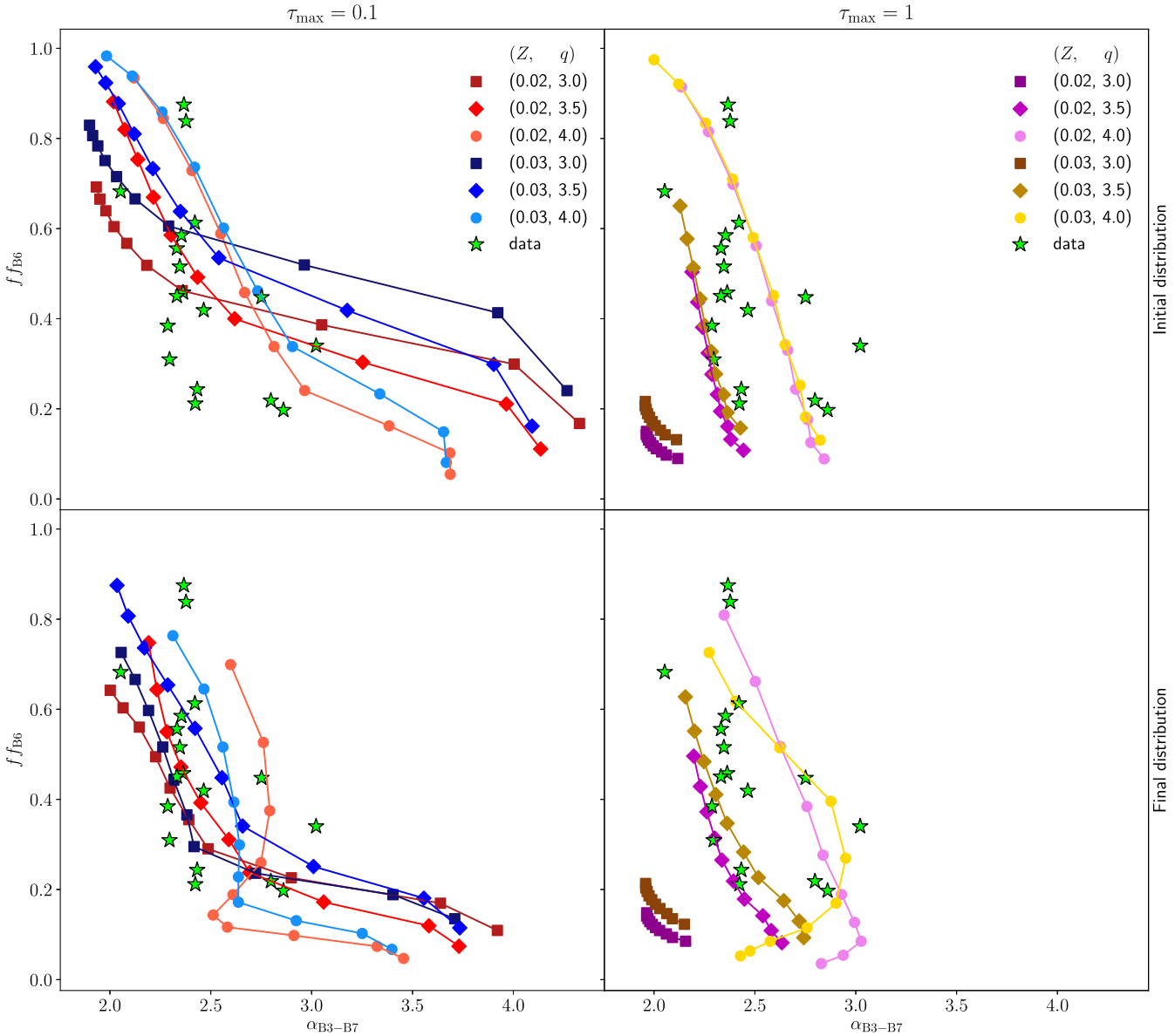

Figure 5. Distribution in the *ff*–α plane of all the simulations performed (see Table 1). The left-hand panels illustrate the distribution in the observable plane for simulations characterized by $\tau_{max} = 0.1$, at the beginning (upper panel) and at the end (lower panel) of the system evolution. The two panels on the right show the same distributions, but for simulations characterized by $\tau_{max} = 1$. The values of the main parameters are indicated in the legend, according to the following rule: the squares correspond to $q = 3$, the diamonds to $q = 3.5$, and the dots to $q = 4$; in the left-hand panel, the shades of red (blue) are used for systems characterized by $Z = 0.02$ ($Z = 0.03$); in the right-hand panel, the shades of pink (brown) are used for systems characterized by $Z = 0.02$ ($Z = 0.03$). In all the panels, the data distribution is illustrated through the green stars.

for cases with $\tau_{max} = 0.1$; this happens because in these models the clumping species are those characterized by β values close to the resonance; thus, by removing these grains from the background emission, the α value must decrease. Therefore, for these cases, the action of streaming instability changes the system optical properties so that they become consistent with the data; thus, the streaming instability can be considered a candidate to explain the data distribution.

We further underline that there are two simulations (T30-Z02-Q3 and T30-Z03-Q3) whose observable quantities barely evolve when clumps form. This behaviour is related to the fact that, in these cases, both the clumping and non-clumping species are relatively big (due to the particular combination of τ_s and q); thus, the creation of clumps does not significantly alter the system opacity.

6 IMPACT OF STREAMING INSTABILITY ON OBSERVATIONS: INTEGRATED MODEL

After studying the local observational properties of clumps, we define in this section an integrated disc model to study the global optical properties of systems undergoing streaming instability.

In the integrated disc model, we assume azimuthal symmetry, and we define a disc characterized by the following gas density profile:

$$\Sigma_g(R) = \Sigma_g(1\,\mathrm{au}) \left(\frac{R}{\mathrm{au}}\right)^{-p}, \tag{31}$$

where $\Sigma_g(1\,\mathrm{au})$ varies between 100 and 3000 g cm^{-2} (note that these values at 1 au correspond to the values used in the local model at the box location) and we define $R_{in} = 0.1$ au and $R_{out} = 70$ au as

Downloaded from https://academic.oup.com/mnras/article/504/1/1495/6188383 by Imperial College London Library user on 25 June 2021

inner and outer radii, respectively. The corresponding dust density profile can be obtained as $\Sigma_d = Z\Sigma_g$, where Z is chosen according to the considered simulation (see Table 1). In this model, the Stokes number is assumed to be constant across the disc [found to be a reasonable approximation in the Birnstiel et al. (2012) two-population model].

We divide the defined disc in $N_{rings} = 100$ 'rings' from $R_{in} = 0.1$ au to $R_{out} = 70$ au, equally spaced on a linear scale. We then use the Σ_g and H_g local values to map simulations into physical units. If the streaming instability is triggered in a particular ring, then the quantities calculated for that ring are those from the end state of the simulation; otherwise, the initial conditions are used.

Once the dust density is obtained, both the opacity and the optical depth are computed at each ring following the same procedure as that used in the local model; in fact, each ring behaves as a single box. In each ring, we compute the flux F_ν^{ring}, then we sum over all the rings to obtain the total flux

$$F_\nu^{TOT} = \sum_{i=1}^{N_{rings}} F_\nu^{ring,i}. \tag{32}$$

It is worth noting that for realistic emissivity profiles, the weighting by surface area ensures a relatively large contribution from the outer disc.

As final step, we compute the observable quantities, which can be simply obtained by using equations (22) and (23) where F_ν^{TOT} is used instead of F_ν.

To explore different scenarios, we consider the following four different disc models:

(1) all the disc is involved in streaming instability;
(2) the inner disc is involved in streaming instability;
(3) the outer disc is involved in streaming instability;
(4) a ring in the disc is involved in streaming instability.

Following the method outlined above, we determine the distribution in the *ff*–α plane for all the four integrated disc models. Since the flux is dominated by the outer disc, we found that in models (2) (where the instability occurs only within 35 au) and (4) (where the instability occurs in a ring of width 10 au located at 35 au), the action of streaming instability hardly affects the flux and, therefore, the observable quantities; for the same reason, streaming instability modifies the observable quantities in models (1) and (3), whose behaviour is similar to each other. Therefore, in the following we show the results only for the 'outer disc' model, where streaming instability is assumed to take place for $R > R_{SI}$ and we choose $R_{SI} = 35$ au.

As in the local model, we compare the distribution in the *ff*–α plane obtained from all the performed simulations to that obtained from the data, and we show the results in Fig. 6. As in Fig. 5, the upper (lower) panels correspond to the initial (final) distributions of system characterized by $\tau_{max} = 0.1$ and 1, on the left and on the right, respectively. The legend is the same as that used in Fig. 5.

As in the local model, the initial conditions partially match the data distribution; in fact, the two distributions overlap in the area characterized by (α, *ff*) $\sim$ (0.6, 2.5); nevertheless, the simulated systems are initially unable to cover the central area where most of the data are located (α, *ff*) $\sim$ (0.4, 2.5). After the action of streaming instability, however, the optically thick fractions decrease, because, as previously explained, the surface density of particles in the optically thin background is reduced by clump formation, reducing the flux and allowing the final distribution to cover the data area that the initial conditions were unable to match. Note that the models do not cover few data located at (α, *ff*) $\sim$ (2.4, 0.8); this can be explained by noticing that *ff* increases and α decreases as the disc radius is reduced, as shown by figs 5 and 7 in Tazzari et al. (2020b). Since our integrated disc models are characterized by a constant disc size ($R_{out} = 70$ au), we expect the low-α high-*ff* data to be reproduced by considering smaller discs (indeed, we verified that they are matched by models with $R_{out} = 35$ au).

It is also worth noticing that in Tazzari et al. (2020a) the spectral index is correlated with radius, suggesting that the large spectral indices of transition discs can be explained if they have large radii for their masses. This result is consistent with the finding by Andrews et al. (2018) that transition discs are large for their flux, which is also reconcilable with the fact that they have a cavity in their mm emission. Such a cavity in the inner disc, however, is not expected to modify significantly the results obtained in this section, as the outer disc is dominant in determining the observable consequences of the action of streaming instability.

We caution that the results might depend on the particular choice of the integrated disc model parameters; see Section 7.2 for a detailed discussion.

Finally, we underline that if we compute the mm fluxes from our models, we find that they are broadly consistent with those observed, if we adopt the same temperature profile and disc sizes as those observed.

7 DISCUSSION

7.1 Influence of model parameters on the distribution (local model)

Although the physics of streaming instability depends only on the parameters chosen in the simulations, the observable quantities also depend on the specific disc model used to convert the simulation dimensionless code units to physical units: The choice of the mass unit influences the grain size, hence the opacity; the local gas density depends on the choice of the box location and the chosen density profile; the temperature profile influences the Planck function.

In Fig. 7, we test the effect on the distribution in the *ff*–α plane of changing the temperature, changing T_0 to 60 K in blue, 120 K in purple, and 240 K in green (corresponding to temperatures of 13, 26, and 52 K at the box location);[5] as an example, we consider simulation T41-Z03-Q4. The shades of each colour represent different local gas densities, logarithmically distributed from $\Sigma_g = 0.5$ to 14.5 g cm^{-2} (the darker the colour, the higher the density). For comparison, the green stars represent the data distribution.

Changing T_0 has no effect on the optically thick fraction, since it only depends on the dust density profile and the opacity (i.e. the grain sizes and their composition), which are independent of T_0 (which only modifies the Planck function). Regarding the spectral index (equation 23), we expect it to be unaffected by T_0 if the emission is in the Rayleigh–Jeans limit (in which case $\alpha = 2 + \beta$); for low T_0, however, the emission is not in the Rayleigh–Jeans regime and

[5]Note that we only calculate the effect of changing temperature on the radiative properties and do not model the effect of changing $\Pi(\propto T^{0.5})$ on the simulations; according to Bai & Stone (2010b), a factor 2 increase of Π over the canonical value causes a modest increase in the dust-to-gas ratio required to trigger the streaming instability.

Downloaded from https://academic.oup.com/mnras/article/504/1/1495/6188383 by Imperial College London Library user on 25 June 2021

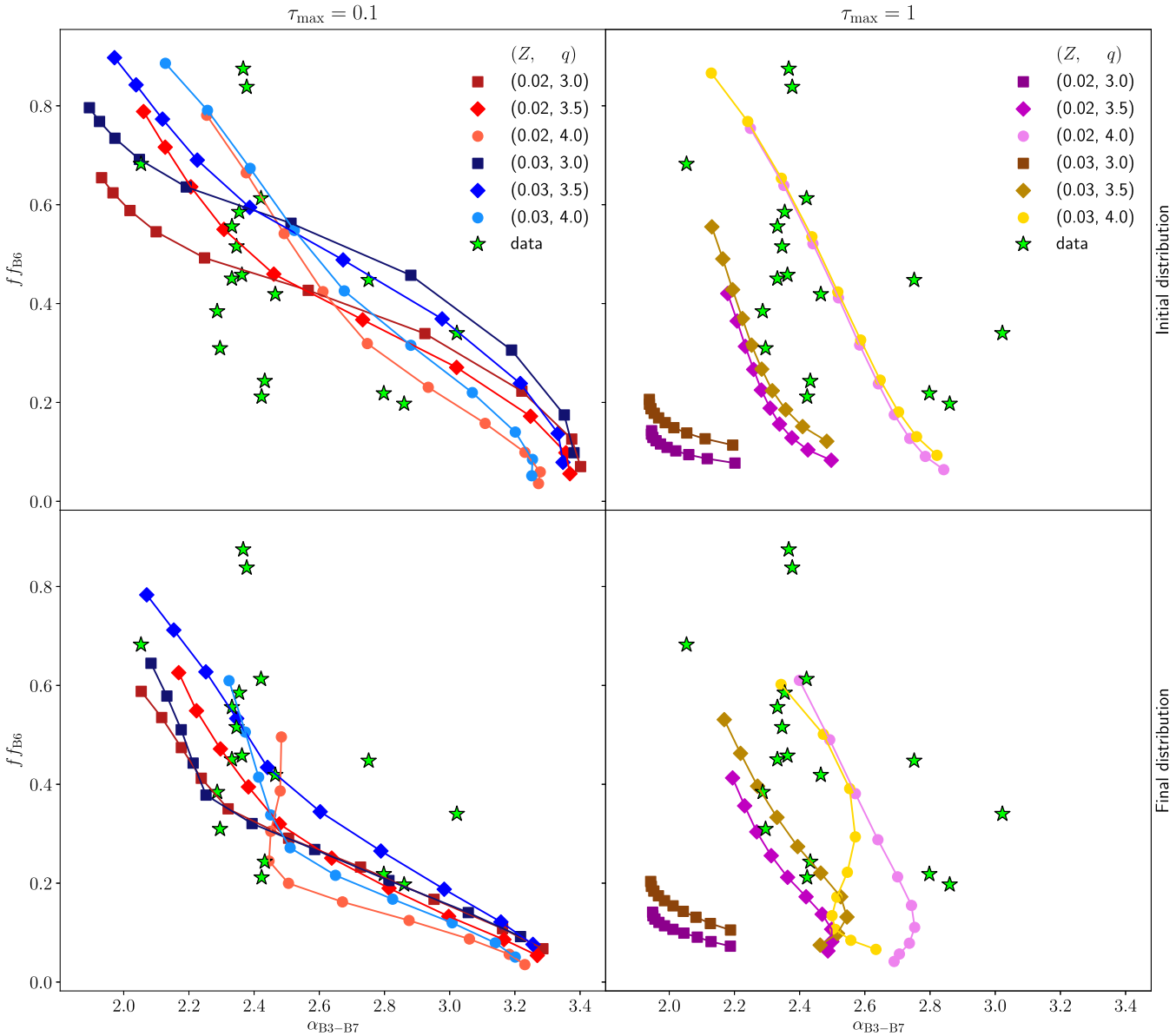

Figure 6. Distribution in the *ff*–α plane of all the simulations performed (see Table 1) applying the outer disc integrated model. The upper panels show the distribution in the plane for the initial condition, for simulations characterized by $\tau_{max} = 0.1$ and 1 in the upper left panel and upper right panel, respectively; the lower panels show the distribution after the system evolution (in the left-hand panel for $\tau_{max} = 0.1$ and in the right-hand panel for $\tau_{max} = 1$). The values of the main parameters are indicated in the legend (following the same rule as in Fig. 5). In all the panels, the data distribution is illustrated through the green stars.

this means that α is lower for lower temperatures due to the fact that the higher frequency emission is beyond the Wien peak, resulting in a lower value of α. We see from Fig. 7 that the effect on the final distribution is relatively small and that the overall distribution is not considerably affected by the choice of T_0.

7.2 Influence of model parameters on the distribution (integrated model)

We also test the influence of the parameter choices in the case of the integrated model, focusing, as an example, on the 'outer disc' model. The main parameters to be studied are R_{out} and R_{SI}.

In the left-hand panel of Fig. 8, we plot three distributions obtained using the method described in Section 6 for different disc outer radii: $R_{out} = 50$ au (blue squares), $R_{out} = 70$ au (purple squares), and $R_{out} = 100$ au (green squares). The value of R_{SI} is modified so that the portion of disc which is involved in streaming instability is always half of the total disc ($R_{SI} = R_{out}/2$). The considered values for the gas density at 1 au are the same regardless of the disc outer radius [$\Sigma_g(1\,\text{au}) = 100$–$3000\,\text{g cm}^{-2}$]. The three obtained distributions are very similar, and the only difference is that smaller discs are slightly optically thicker; in fact, the outer disc portion (which dominates the flux) in smaller discs is optically thicker than that in a bigger disc (see equation 31); therefore, overall the disc is expected to be optically thicker.

In the right-hand panel of Fig. 8, we test the effect of changing R_{SI} when $R_{out} = 70$ au is fixed. In particular, we consider $R_{SI} = 15$ au (blue squares), $R_{SI} = 35$ au (purple squares), and $R_{SI} = 55$ au (green squares). We notice that when R_{SI} is lower, and thus more of

Downloaded from https://academic.oup.com/mnras/article/504/1/1495/6188383 by Imperial College London Library user on 25 June 2021

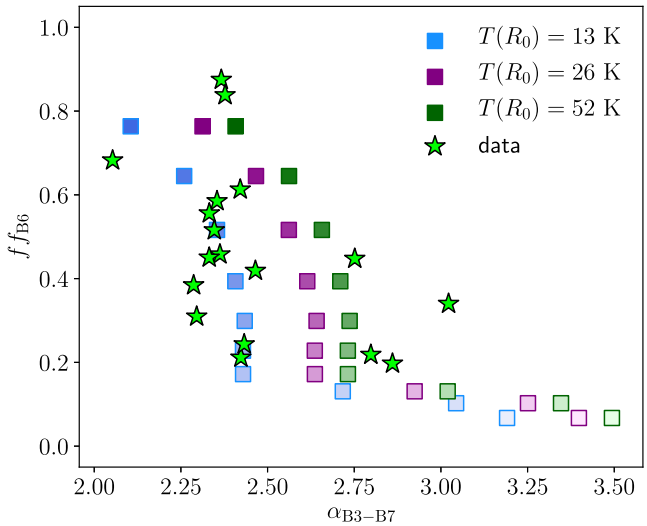

Figure 7. Distribution in the *ff*–α plane at a box location of 35 au for simulation T41-Z03-Q4 considering different temperature scalings: $T_0 = 60$ K in blue, $T_0 = 120$ K in purple, and $T_0 = 240$ K in green (local temperatures of 13, 26, and 52 K). The shades of colours correspond to different values for local Σ_g (logarithmically distributed in the interval 0.5–14.5 g cm^{-2}). The green stars represent the data distribution by Tazzari et al. (2020a).

the disc participates in the streaming instability, the optically thick fractions tend to be slightly lower and the bunching towards a smaller range of α (see left-hand hand panel of Fig. 2) also becomes more pronounced.

Overall, the distributions shown in Fig. 8 are not significantly influenced by the choice of either R_{out} or R_{SI} in the range considered. Therefore, we can state that the result obtained in Fig. 6 is reasonably model independent, provided that the streaming instability is operating over a region of the disc that contributes significantly to the total emission at mm wavelengths.

7.3 Composition and porosity

In this paper, we analysed the optical properties of the simulated systems by considering the composition for dust grains similar to that used in Tazzari et al. (2016) (which corresponds to the composition labelled as 'Zubko' in Birnstiel et al. 2018). However, it is important to discuss how the results would be affected by different compositional choices.

We first note, by combining equations (4) and (19), that at fixed dust-to-gas ratio, the Stokes number depends on the maximum grain size, optical depth, and opacity via

$$\tau_s \propto \frac{k_\nu^{avg}}{\tau_\nu} a. \tag{33}$$

We found that, in our models, the streaming instability was successful in improving the match to the properties of observed discs on account of the changes in optical depth and spectral index effected when the maximum grain size is close to the opacity resonance. For the compositions adopted here, when the optical depth fraction is several tens of per cent (as in observed systems) and a is close to the opacity resonance, then the Stokes number is in the range where the streaming instability is strong. We can estimate the effect of using, for example, the DSHARP composition (see the case labelled as 'default' in Birnstiel et al. 2018). From the top panel in fig. 10 of Birnstiel et al. (2018), we observe that the DSHARP opacity is lower than the 'Zubko' one (approximately by a factor of 20) while the β peak (middle panel) is located at higher a values (approximately by a factor of 4). This means that for the DSHARP composition the Stokes number corresponding to the resonance at the same optical depth would be around a factor of 5 less than what we have simulated in this paper. It remains to be seen whether the streaming instability is

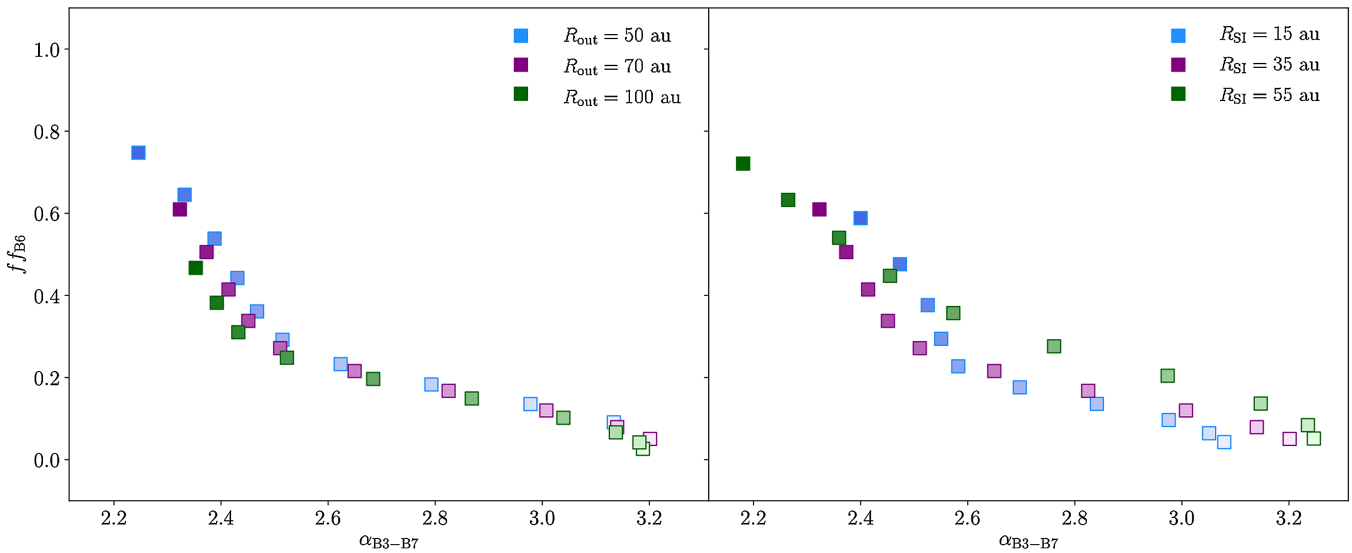

Figure 8. Distributions in the *ff*–α plane for simulation T41-Z03-Q4, using the 'outer disc' integrated model. The left-hand panel shows three distributions obtained using different outer disc radii: $R_{out} = 50$ au (blue squares), $R_{out} = 70$ au (purple squares), and $R_{out} = 100$ au (green squares); in all the three cases, we rescale R_{SI} so that in all models half of the disc is involved in streaming instability ($R_{SI} = R_{out}/2$). The range of gas density at 1 au is the same for all the three cases: $\Sigma_g(1\,\text{au}) = 100$–$3000$ g cm^{-2}. The right-hand panel shows three distributions obtained by fixing the outer radius $R_{out} = 70$ au and changing the radius dividing the area undergoing streaming instability from the area where streaming instability does not take place: blue squares correspond to $R_{SI} = 15$ au; purple squares to $R_{SI} = 35$ au; and green squares to $R_{SI} = 55$ au. In both the plots, the colours of the squares vary their intensity according to the density of the corresponding disc (the higher is the disc density, the darker is the colour).

Downloaded from https://academic.oup.com/mnras/article/504/1/1495/6188383 by Imperial College London Library user on 25 June 2021

sufficiently strong at these lower Stokes numbers to have a significant effect on disc radiative properties.

Likewise, we note that if, instead, porous grains are employed, the peak in β associated with the opacity resonance virtually disappears (see middle panel of fig. 10 in Birnstiel et al. 2018) and thus the streaming instability would have little impact on mm emission from discs. In the absence of the streaming instability, Tazzari et al. (2020b) showed that the data in Lupus require lower β values than can be produced by porous grains. Thus, since we find that the streaming instability does little to the radiative properties of discs in this case, we are led to disfavour the hypothesis of porous grains.

8 CONCLUSIONS

In this paper, we simulated the action of streaming instability by performing 12 2D shearing box simulations with multiple grain sizes using the ATHENA code. By comparing the results from our simulations to observations in Lupus by Tazzari et al. (2020a,b), we found that the action of streaming instability is overall consistent with the integrated emission from discs at mm wavelengths.

Analysis of dust density profiles after clump formation shows that the largest particles participate significantly in clumping, whereas the smallest ones remain almost uniformly in the background. Streaming instability thus affects the emission properties of discs in cases where grains towards the upper end of the grain size distribution exhibit a steep dependence of opacity, and its wavelength dependence, on grain size. Such a steep dependence is associated, in the case of compact grains, with the opacity resonance at a grain size around a few tenths of a mm.

We explored the effect of the streaming instability on the location of models in the *ff*–α (optical depth fraction versus spectral index) plane. The instability always reduces the optical depth fraction, because the effect of clumping is to reduce the emission from those grains that are translated from optically thin to optically thick regions [in agreement with the finding by Stammler et al. (2019) that the streaming instability reduces the system's optical depth]. The spectral index can evolve in either direction depending on whether the maximum grain size is above or below the size corresponding to the opacity resonance. The net effect is to drive modelled disc systems towards a relatively narrow range of spectral indices (around $\sim$2.5) that agrees well with the observed distribution of discs in the *ff*–α plane (see Fig. 5).

Finally, we remark that although we have investigated the specific scenario of clump generation by streaming instability, our results are likely to apply, at least qualitatively, to any situation where clumping predominantly affects the largest grains. Clumping is likely strongest for large particles in any effective clumping mechanism, as is the case for trapping by spiral arms in self-gravitating discs (as long as $\tau_s \lesssim 1$; Booth & Clarke 2016), pressure maxima created by planets, and vortices. Our primary result (that clumping reduces the optically thick fraction and brings systems to a relatively narrow range of spectral index values) is therefore likely to be of general applicability.

ACKNOWLEDGEMENTS

We thank the referee for his comments that have helped us to improve the clarity of the paper, and Marco Tazzari for providing us with the data. CES thanks Peterhouse for a Ph.D. studentship and RAB and CJC acknowledge support from the Science and Technology Facilities Council (STFC) consolidated grant ST/S000623/1. This work has also been supported by the European Union's Horizon 2020 research and innovation programme under the Marie Sklodowska-Curie grant agreement number 823823 (DUSTBUSTERS).

DATA AVAILABILITY

The data underlying this article were provided by Tazzari et al. (2020a,b) by permission. Data will be shared on request to the corresponding author with permission of Tazzari et al. (2020a,b).

REFERENCES

Adachi I., Hayashi C., Nakazawa K., 1976, Prog. Theor. Phys., 56, 1756
Andrews S. M. et al., 2018, ApJ, 869, L41
Ansdell M. et al., 2016, ApJ, 828, 46
Ansdell M. et al., 2018, ApJ, 859, 21
Armitage P. J., 2007, preprint (arXiv:astro-ph/0701485)
Bai X.-N., Stone J. M., 2010a, ApJS, 190, 297
Bai X.-N., Stone J. M., 2010b, ApJ, 722, 1437
Bai X.-N., Stone J. M., 2010c, ApJ, 722, L220
Birnstiel T., Klahr H., Ercolano B., 2012, A&A, 539, A148
Birnstiel T., Fang M., Johansen A., 2016, Space Sci. Rev., 205, 41
Birnstiel T. et al., 2018, ApJ, 869, L45
Booth R. A., Clarke C. J., 2016, MNRAS, 458, 2676
Brauer F., Dullemond C. P., Henning T., 2008, A&A, 480, 859
Carrera D., Johansen A., Davies M. B., 2015, A&A, 579, A43
Chiang E., Youdin A. N., 2010, Annu. Rev. Earth Planet. Sci., 38, 493
Dominik C., Tielens A. G. G. M., 1997, ApJ, 480, 647
Dominik C., Paszun D., Borel H., 2016, preprint (arXiv:1611.00167)
Draine B. T., 2003, ARA&A, 41, 241
Drążkowska J., Alibert Y., Moore B., 2016, A&A, 594, A105
Dullemond C. P. et al., 2018, ApJ, 869, L46
Epstein P. S., 1924, Phys. Rev., 23, 710
Garaud P., Meru F., Galvagni M., Olczak C., 2013, ApJ, 764, 146
Gole D. A., Simon J. B., Li R., Youdin A. N., Armitage P. J., 2020, ApJ, 904, 132
Henning T., Stognienko R., 1996, A&A, 311, 291
Huang J. et al., 2018, ApJ, 869, L42
Johansen A., Youdin A., 2007, ApJ, 662, 627
Johansen A., Oishi J. S., Mac Low M.-M., Klahr H., Henning T., Youdin A., 2007, Nature, 448, 1022
Kobayashi H., Tanaka H., 2018, ApJ, 862, 127
Kobayashi H., Tanaka H., Okuzumi S., 2016, ApJ, 817, 105
Kokubo E., Ida S., 1996, Icarus, 123, 180
Krapp L., Benítez-Llambay P., Gressel O., Pessah M. E., 2019, ApJ, 878, L30
Laibe G., Price D. J., 2014, MNRAS, 444, 1940
Li R., Youdin A. N., Simon J. B., 2018, ApJ, 862, 14
Lissauer J. J., 1993, ARA&A, 31, 129
Liu B., Ji J., 2020, Res. Astron. Astrophys., 20, 164
Ormel C. W., Dullemond C. P., Spaans M., 2010, Icarus, 210, 507
Papaloizou J. C. B., Terquem C., 2006, Rep. Prog. Phys., 69, 119
Pinte C., Laibe G., 2014, A&A, 565, A129
Rafikov R. R., 2003, AJ, 125, 942
Safronov V. S., Zvjagina E. V., 1969, Icarus, 10, 109
Schaffer N., Yang C.-C., Johansen A., 2018, A&A, 618, A75
Squire J., Hopkins P. F., 2020, MNRAS, 498, 1239
Stammler S. M., Drążkowska J., Birnstiel T., Klahr H., Dullemond C. P., Andrews S. M., 2019, ApJ, 884, L5
Stone J. M., Gardiner T. A., Teuben P., Hawley J. F., Simon J. B., 2008, ApJS, 178, 137
Takeuchi T., Lin D. N. C., 2002, ApJ, 581, 1344
Tazzari M. et al., 2016, A&A, 588, A53
Tazzari M. et al., 2020a, preprint (arXiv:2010.02248)
Tazzari M., Clarke C. J., Testi L., Williams J. P., Facchini S., Manara C. F., Natta A., Rosotti G., 2020b, preprint (arXiv:2010.02249)
Umurhan O. M., Estrada P. R., Cuzzi J. N., 2020, ApJ, 895, 4
Warren S. G., Brandt R. E., 2008, J. Geophys. Res. (Atmos.), 113, D14220
Weidenschilling S. J., 1977, MNRAS, 180, 57

Downloaded from https://academic.oup.com/mnras/article/504/1/1495/6188383 by Imperial College London Library user on 25 June 2021

Yang C.-C., Johansen A., 2014, ApJ, 792, 86
Yang C.-C., Johansen A., Carrera D., 2017, A&A, 606, A80
Youdin A. N., Goodman J., 2005, ApJ, 620, 459
Youdin A., Johansen A., 2007, ApJ, 662, 613
Zhu Z., Yang C.-C., 2021, MNRAS, 501, 467
Zubko V. G., Mennella V., Colangeli L., Bussoletti E., 1996, MNRAS, 282, 1321

APPENDIX A: CONVERGENCE

Since we are interested in the changes of optical properties before and after the action of streaming instability, we must ensure that at the end of our running time our simulations have converged. We therefore computed for each simulation the observable quantities as a function of time, and we considered the simulation as converged when α and *ff* stopped to increase/decrease. In Fig. A1, we show, as an example, the variation of the spectral index with time for simulation T30-Z03-Q4: In the first 800 dynamical times α increases considerably, and then it stabilizes on a nearly constant value. We performed this convergence test for all the simulations, finding that the most of simulations have converged after 1500 Ω^{-1}, apart from a few simulations (simulations T41-Z02-Q4, T41-Z03-Q4, T30-Z02-Q3, and T30-Z03-Q3) that required a longer evolution to reach convergence (2000 Ω^{-1}).

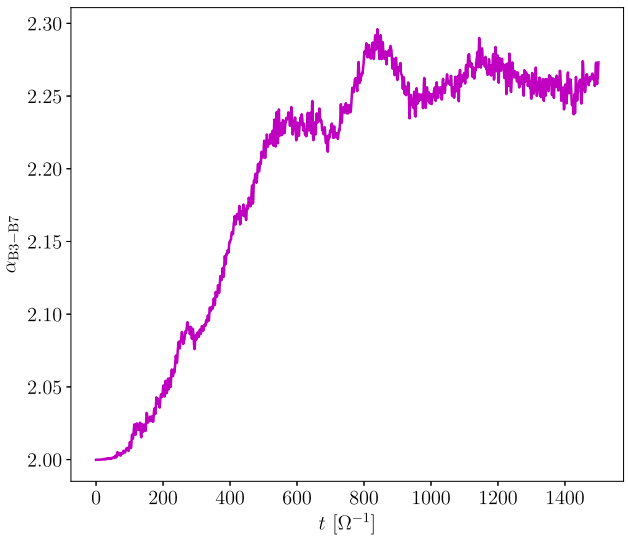

Figure A1. Spectral index as a function of time for simulation T30-Z03-Q4, considering the standard disc model with local gas density $\Sigma_g = 14.5$ g cm^{-2}.

APPENDIX B: OPACITY

Considering as an example simulation T41-Z03-Q4, we explain here the details of the method applied to compute the size averaged opacity for our simulations. The method can be split into three phases: (1) We compute the single grain opacity, using Birnstiel et al. (2018) code; (2) we interpolate over the grain size interval that each simulated grain represents (equation 17); and (3) we compute the size-averaged opacity (equation 18). To test whether our computation works properly, we compute the opacity index β as a function of the maximum grain size $a_{\rm max}$ and we compare it to the same quantity obtained with Birnstiel et al. (2018) code.

In the left-hand panel of Fig. B1, the magenta line shows β obtained by considering a simulation characterized by seven particle species and without operating the grain interpolation. The thick grey line shows the result obtained from Birnstiel et al. (2018) code (as well as in the other two panels). This computation is clearly unable to return the correct opacity, as the low number of species and the absence of grain size interpolation cause strong oscillations. By increasing the number of particle species to 28 (central panel), we note a considerable improvement in the computation of opacity, since the majority of oscillations disappear; nevertheless, at high $a_{\rm max}$, β seems to be underestimated. Once we introduce also the size grain interpolation (right-hand panel), we are finally able to recover precisely the correct shape of $\beta - a_{\rm max}$. This analysis allowed us to choose the correct number of particle species to insert in our simulation (28 species) and to verify that equation (17) is needed in order to compute the opacity properly.

In Fig. B2, we applied the method outlined above to the cases $q = 3$ (magenta line), $q = 3.5$ (cyan line), and $q = 4$ (violet line). The thin lines refer to our computation, and the thick translucent ones refer to the corresponding result obtained through Birnstiel et al. (2018) code. Even though for small $a_{\rm max}$, the three cases behave similarly, they differ significantly among each other for the peak height and the value for big $a_{\rm max}$. In particular, for big grains, the opacity variation with frequency is steeper and steeper as q increases.

Downloaded from https://academic.oup.com/mnras/article/504/1/1495/6188383 by Imperial College London Library user on 25 June 2021

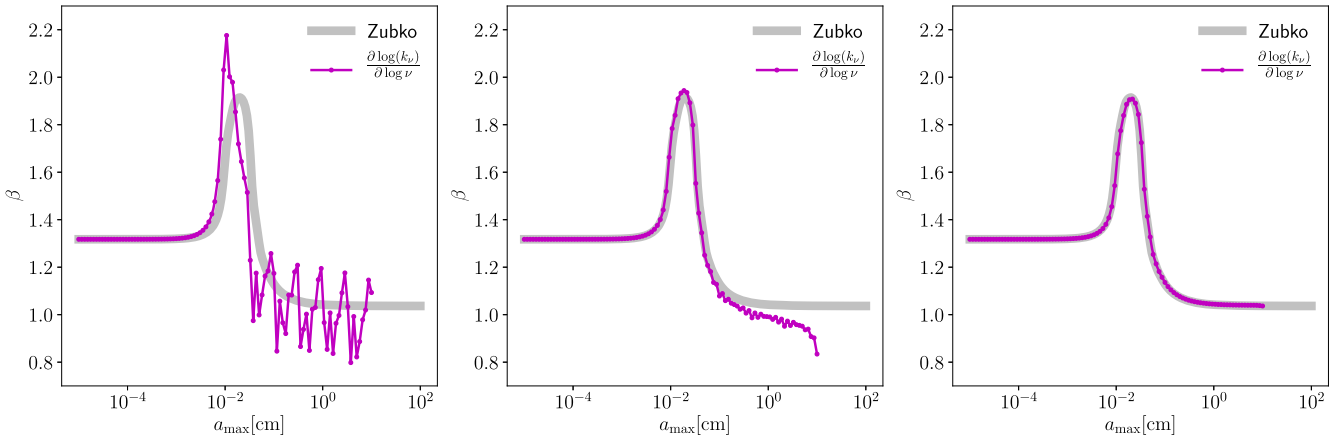

Figure B1. Opacity index as a function of the maximum grain size for different models, obtained from simulation T41-Z03-Q4. The grey line is the result obtained from Birnstiel et al. (2018) code; the magenta line is the result of our computation. The left-hand panel shows the result when we consider the single grain opacity and seven particle species; the middle panel shows the result when we interpolate the grain distribution using 28 particle species; the right-hand panel shows the result when we consider that each grain represents a set of grains and we extrapolate the distribution to include the low-mass grains.

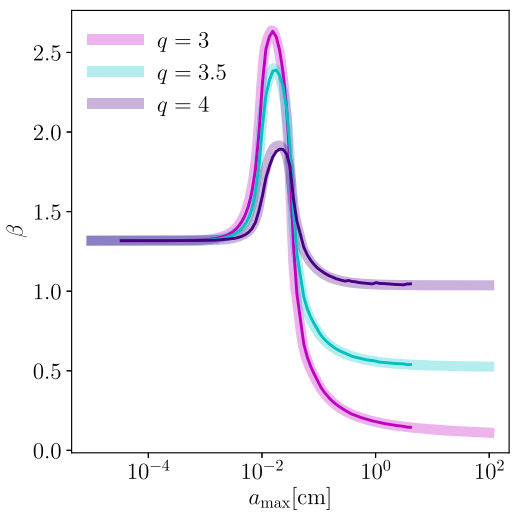

Figure B2. Opacity index as a function of the maximum grain size, for different grain size distributions: $q = 3$ (magenta), $q = 3.5$ (cyan), and $q = 4$ (violet). The thick translucent lines correspond to the values obtained through Birnstiel et al. (2018) code; the thin solid lines correspond to the values computed using our sets of dust grain distributions.

APPENDIX C: TOY MODEL

In Section 5.1, we used a toy model to illustrate how the optical properties of clumping particles affect the increase/decrease in α. Here, we show that the toy model is effective in reproducing the distribution in the *ff*–α plane of simulated systems.

We compute for each simulation the level of clumping for each particle species through the mean density ratio (i.e. we compute the dust density for each particle species and average that over all the particles), then we use the result to identify the clump area as the area where the final mean density ratio is higher than the initial one, and finally we obtain p by using equation (28). The result is shown in Fig. C1.

We then use the values of p computed above to mimic clump formation of each particle species[6] through equations (28) and (27) and we compute the corresponding distribution in the *ff*–α plane. We test the toy model by applying it to the initial conditions of simulations plotted in Fig. 2 and we show the results in Fig. C2 (the panels, from left to right, correspond to the panels in Fig. 2). By comparing Figs C2 to 2, we can notice that the behaviour of the observable quantities in the toy model is similar to that obtained through the actual simulations; this confirms that both the definition used to obtain p in Fig. C1 and the method of mimic clump formation by redistributing the particles are effective in reproducing the observable quantities.

[6]Note that the simplified approach used in Section 5.1, in which we arbitrarily split the particles into clumping/non-clumping species, is useful to explain the different behaviours of α, but it cannot reproduce the distribution in the *ff*–α plane precisely.

Downloaded from https://academic.oup.com/mnras/article/504/1/1495/6188383 by Imperial College London Library user on 25 June 2021

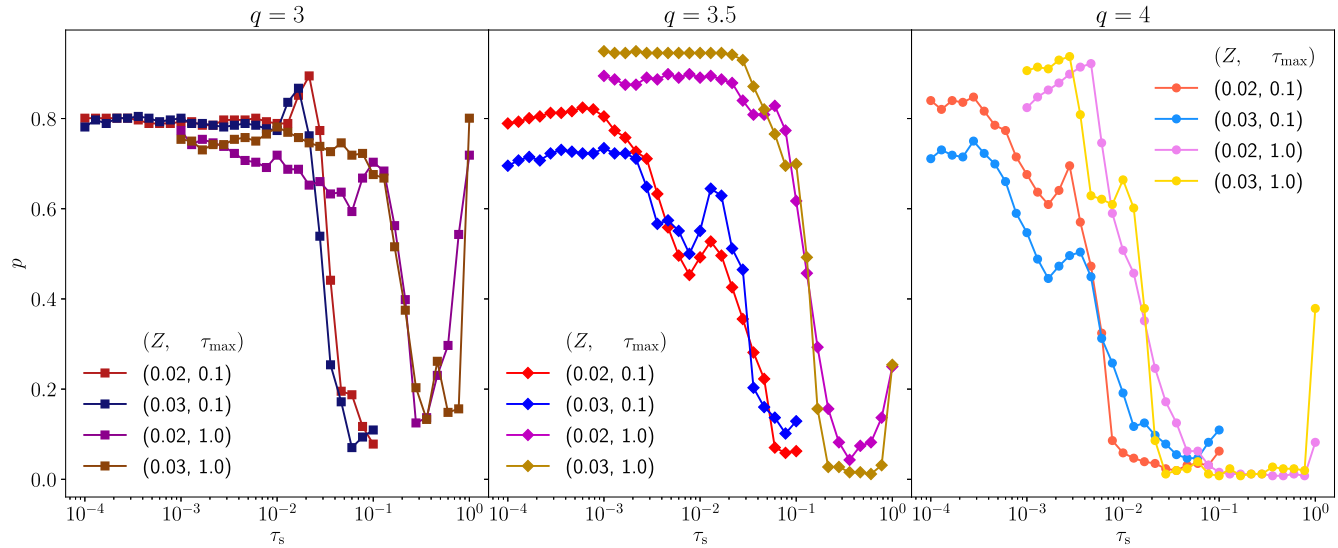

Figure C1. Parameter p as a function of the particle species Stokes number τ_s for all the simulations performed. The results are split into three groups depending on their q parameter: $q = 3$ in the left-hand panel, $q = 3.5$ in the central panel, $q = 4$ in the right-hand panel.

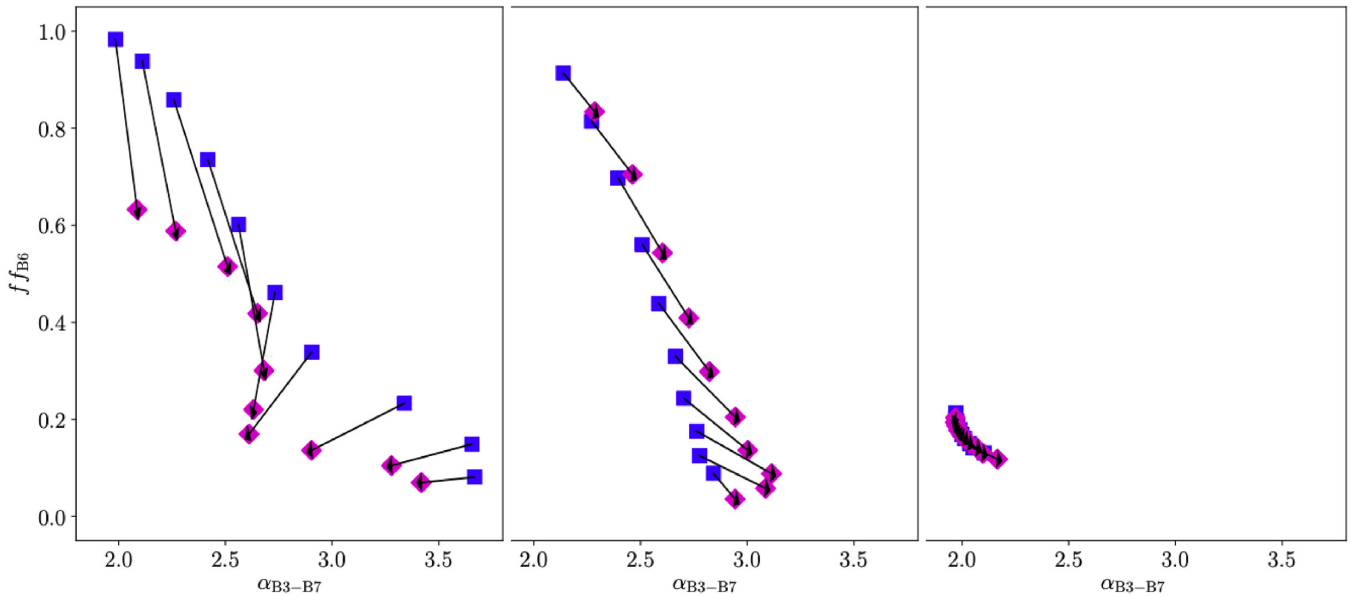

Figure C2. Distribution in the ff–α plane obtained applying the toy model to systems characterized by the same parameters as simulations considered in Fig. 2: T41-Z03-Q4 (left-hand panel), T30-Z02-Q4 (central panel), and T30-Z03-Q3 (right-hand panel).

This paper has been typeset from a TEX/LATEX file prepared by the author.

Downloaded from https://academic.oup.com/mnras/article/504/1/1495/6188383 by Imperial College London Library user on 25 June 2021